Collective bacterial motion drives interfacial waves and shape dynamics in phase-separated droplets

Kan Chang, 1,* Yulin Li, 2,* Ming Yuan, 1 Masaki Sano, 1 Zhihong You, 2,† and H. P. Zhang 1,‡

1 School of Physics and Astronomy, Institute of Natural Sciences and MOE-LSC,

Shanghai Jiao Tong University, Shanghai 200240, China

2 Fujian Provincial Key Laboratory for Soft Functional Materials Research,

Research Institute for Biomimetics and Soft Matter,

Department of Physics, Xiamen University, Xiamen, Fujian 361005, China

(Dated: November 18, 2025)

Liquid—liquid phase separation governs a broad spectrum of phenomena in biology, physics, and materials science. While traditionally explored in equilibrium contexts, growing evidence underscores the transformative role of active components, such as motor proteins, enzymatic catalysts, and synthetic microswimmers, in modulating the dynamics of phase-separated systems. Here, we encapsulate motile bacteria within phase-separated aqueous droplets to examine how internal activity shapes interfacial behavior. By tuning bacterial density, we control the magnitude of active stresses at the droplet interface. At low activity, we observe scale-dependent interfacial fluctuations featuring propagative wave modes. Remarkably, despite the low Reynolds number regime, these waves arise from an effective inertial response that emerges when bacterial active stresses balance viscous dissipation. At high activity, droplets exhibit pronounced deformation that exceeds the Rayleigh–Plateau instability threshold, accompanied by enhanced motility that accelerates coarsening. Our findings demonstrate how active stresses can reshape morphology and dynamics in multiphase systems, offering new insights into the physics of internally driven phase-separated fluids.

Introduction

Interfaces are central to living matter. From cell membranes and organelle surfaces to biomolecular condensates formed by liquid—liquid phase separation (LLPS), they establish dynamic boundaries that compartmentalize reactions, mediate material exchange, and enable adaptation to changing environments [1–16]. These interfaces are inherently out of equilibrium: they are continually remodeled by active processes such as actindriven cell motility [5–7], metabolic and cytoskeletal forces that drive red-blood-cell flickering [8–13], and actomyosin-mediated remodeling of phase-separated condensates [14–16]. Together, these systems illustrate that biological interfaces are not passive materials, but active surfaces whose geometry and fluctuations are continuously sculpted by internal force generation.

Motivated by these observations, bottom-up model systems have been developed to isolate and reconstitute the physical principles underlying active interface dynamics [17–29]. Recent experiments using microtubule-kinesin active nematics demonstrated that activity can drive flat liquid-liquid interfaces and phaseseparating fronts far from equilibrium, leading to violation of equipartition [17], propagating interfacial modes at vanishing Reynolds number [17], symmetry-broken shapes [19], and arrested phase separation [18]. Closed vesicles and droplets with internal activity, mimicking cells, have also been investigated. In vesicles, internal stresses strongly remodel elastic lipid membranes, producing large-amplitude, nonequilibrium deformations [20-25]. By contrast, liquid droplets possess purely fluid interfaces governed by surface tension rather than membrane elasticity. Theory and simulations predict that internal activity in such droplets can drive spontaneous shape changes, motility, and even division-like events [30–37]. However, despite this rich theoretical landscape, experimental realizations of closed, liquid—liquid droplets actively deformed from within remain scarce [26–29].

Here, we introduce an experimental platform for 3D phase-separated droplets encapsulating dense suspensions of motile bacteria. Combining experiments, simulations, and theory, we show that internal activity can compensate viscous dissipation in the surrounding passive phase, creating a viscosity-matching regime in which the interface becomes effectively underdamped and supports propagating capillary-like waves, thereby restoring effective inertia to an otherwise overdamped Stokesian system. At higher activity, bacterial motility overwhelms capillarity, driving multiscale interfacial deformations ranging from cell-scale filaments to tens-of-micron protrusions. These shape changes, in turn, remodel dropletscale dynamics, giving rise to active random walks and activity-mediated coarsening. Together, these results uncover a continuum of active interfacial modes in living droplets, and point toward strategies for engineering motility-powered artificial cells through activity-induced mechanical stresses [38–42].

Bacteria-polymer active mixtures

Our experimental system consists of a ternary mixture of polyethylene glycol (PEG), dextran, and motile E. coli bacteria (Fig. 1a). In the absence of bacteria, the PEG/dextran solution in our experiments undergoes liquid-liquid phase separation, forming dextran-rich

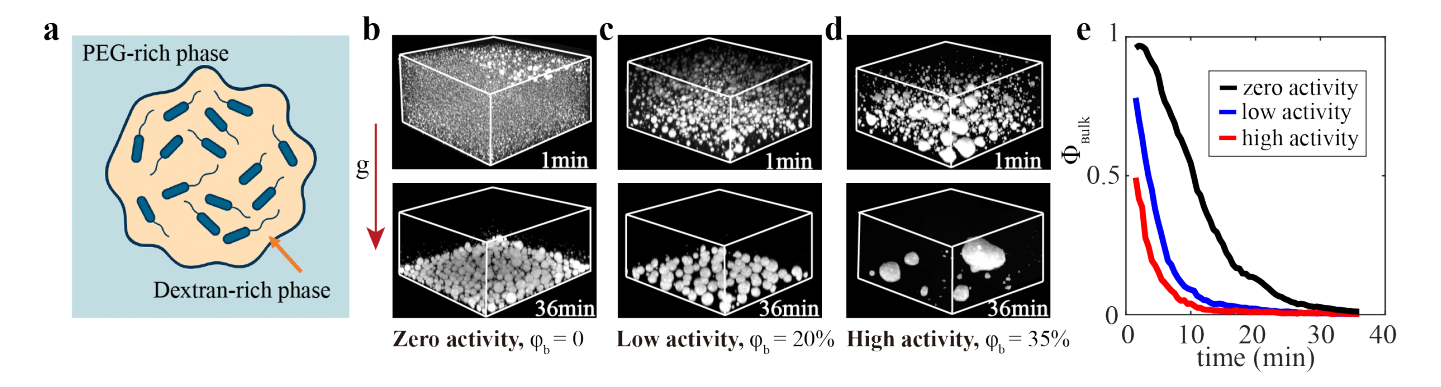


FIG. 1. Phase separation and sedimentation dynamics. (a) Schematic illustration of an active bacterial droplet. (b–d) Confocal images at the initial (T=1 min, top) and final (T=36 min, bottom) stages of coarsening and sedimentation for (b) the control case without bacteria, (c) the low-activity case $(\varphi_b=20\%)$, and (d) the high-activity case $(\varphi_b=35\%)$. Field of view: $330 \ \mu\text{m} \times 330 \ \mu\text{m} \times 200 \ \mu\text{m}$. Fluorescence highlights the dextran-rich phase. (e) Time evolution of the volume fraction of the droplet in bulk, excluding those touching the substrate. See SI for measurements of liquid densities, viscosities, contact angles, and surface tension.

droplets with a surface tension of 7 μ N/m (Methods). As shown in Fig. 1b and Movie S1, these fluorescently labeled dextran-rich droplets coarsen and sediment over time. Introducing motile bacteria into the mixture leads to complete partitioning of the cells into the more hydrophilic dextran-rich phase [43, 44]. We use two bacterial volume fractions, defined as the ratio of the bacteria volume to that of dextran-rich droplets, namely, $\varphi_{\rm b}$ = 20% in Fig. 1c and $\varphi_{\rm b} = 35\%$ in Fig. 1d. Bacterial motion actively deforms and displaces the droplets, which dramatically accelerates sedimentation: all bacteria-laden droplets reach the chamber bottom within 10 minutes, as shown in Fig. 1e. Once settled, these droplets, with radii R ranging from tens to hundreds micrometers, serve as confined environments in which we directly quantify bacterial motion and probe the complex interfacial dynamics that emerge at the liquid-liquid phase boundary.

Activity-driven interfacial fluctuations

At a bacterial volume fraction $\varphi_b = 20\%$, dextranrich droplets remain approximately spherical (Fig. 2a, Fig. S1a and Movie S2). We image bacterial motion on the equatorial plane of the droplets. Fig. 2a–Fig. 2b and Movie S3 show the emergence of collective bacterial flows within two representative droplets. From the measured velocity fields, we compute the velocity auto-correlation function and extract a characteristic correlation length ℓ_v (Fig. S11a). The value of ℓ_v is on the order of tens of micrometers and grows sublinearly with droplet size R (Fig. S11b), consistent with recent experimental observations of confined bacterial turbulence [45, 46].

Bacterial flow leads to pronounced fluctuations of droplet interface, as shown in Fig. 2a–Fig. 2b and Movie S3, which are negligible for droplets with the similar size in thermal equilibrium. To quantify the interface fluctuations, we parameterize the equatorial contour at

time t as $r(\varphi,t)$, where φ is the azimuthal coordinate (Fig. S3). We then compute the temporally averaged fluctuation spectrum $S(k) = \langle |\hat{u}_k|^2 \rangle$, with \hat{u}_k the spatial Fourier transform of the radial deformation $r(\varphi, t)$ [47]. Fig. 2c shows the fluctuation spectra of four representative droplets. The spectra show a clear change in scaling behavior at the characteristic wavevector of $1/\ell_v$, from a k^{-2} dependence at small k to a k^{-4} dependence at large k. These scale-dependent behaviors underscore how nonequilibrium driving fundamentally redistributes interfacial energy among modes [17, 20, 21, 24, 27], in contrast to the equilibrium-like equipartition observed in passive droplets or vesicles [47–50]. Temporal behavior of the fluctuations can be characterized by the normalized dynamic structure factor $S_n(k,\omega)$ (Methods), which exhibits peaks at nonzero frequencies for small wavenumbers (Fig. 2d). This indicates the presence of propagating wave modes, consistent with the kymographs in Fig. S6a. As k increases, $S_n(k,\omega)$ no longer displays distinct wave peaks. This transition occurs at a k_c , marked by the dashed line in Fig. 2d, which approximately corresponds to the scale of the velocity correlation length ℓ_v .

To gain further insight into the spatial and temporal dynamics of active droplets, we perform numerical simulations of a simplified model of an active–passive liquid mixture that nonetheless captures all essential features. Our model couples the Cahn–Hilliard equation and the Toner–Tu–Swift–Hohenberg (TTSH) equation (Methods), which describe phase separation and bacterial motion, respectively [51–55]. The simulation settings and selection of model parameters are discussed in Sec. S2 in the SI. Our simulations reproduce both the active collective flows and the interfacial fluctuations observed experimentally (Fig. 2e, Fig. 2f). To analyze the interface dynamics, we represent the droplet interface as $r(\theta, \varphi)$, where θ and φ are the polar and azimuthal angles, re-

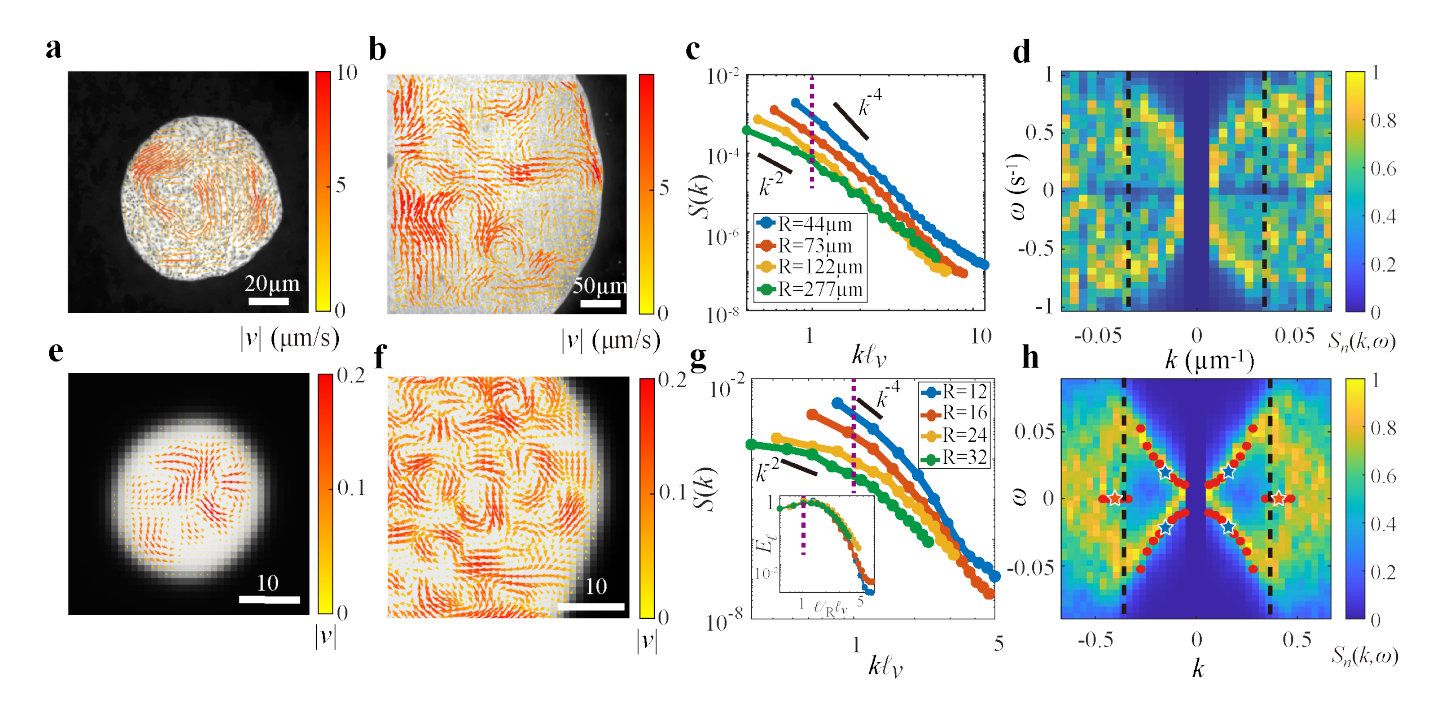


FIG. 2. Shape dynamics of active droplets measured in experiments (top) and simulations (bottom). (a,b) Experimental bacterial flow fields measured on the equatorial plane in two droplets with different radii: (a) $R=39.6~\mu m$ and (b) $R=273~\mu m$. (c) Fluctuation spectra, S(k), measured in four droplets. The horizontal axis is normalized by the corresponding flow correlation lengths, ℓ_v ; the dashed line marks $k\ell_v=1$. (d) Normalized dynamic structure factor, $S_n(k,\omega)$, measured in a droplet with $R=226~\mu m$. The dashed line marks the cutoff wavevector k_c . (e,f) Numerical bacterial flow fields measured on the equatorial plane in two simulated droplets with different radii (in simulation units): (e) R=12 and (f) R=32. (g) Fluctuation spectra, S(k), obtained from simulations of four droplets. Inset: Mean interfacial energy E_ℓ as a function of $\ell/R \cdot \ell_v$, averaged over m. The dashed lines mark $k\ell_v=1$. (h) Normalized dynamic structure factor, $S_n(k,\omega)$, for a simulated droplet with R=32. The dashed line marks the cutoff wavevector k_c . Red dots denote characteristic frequencies extracted from simulations with specific initial conditions (see Fig. 3) and stars correspond to the two curves with $\ell=5, m=0$ (blue) and $\ell=13, m=0$ (orange) in Fig. 3(b). The zero frequency points correspond to damping conditions. All experimental data are obtained in droplets with $\varphi_b=20\%$, and all simulation parameters are described in SI Sec. S2.

spectively. We then decompose it into spherical harmonics, $Y_{\ell,m}(\theta,\varphi)$, specified by two indices, (ℓ,m) , allowing us to compute the three-dimensional fluctuation spectra and the mean interfacial energy spectrum E_{ℓ} (Fig. 2g inset, Fig. S4a-b). As shown in the inset of Fig. 2g, E_{ℓ} measured in droplets of different radii R collapses onto a single curve when plotted as a function of ℓ/R , exhibiting a clear peak at the characteristic wavevector $1/\ell_v$. This peak reflects the scale at which active flows inject energy into the interface, corresponding to the velocity correlation length ℓ_v [56–58]. As detailed in Sec. S3(A.3), the spherical harmonic fluctuation spectra can be projected onto the equatorial plane to yield the fluctuation spectra S(k) shown in Fig. 2g, which are consistent with the experimental results in Fig. 2c and exhibit the same transition in scaling behavior at $1/\ell_v$. Together, the simulations and experiments reveal a coherent physical picture: active flows inject energy into the interface peaked at the correlation length scale ℓ_v . This injected energy drives large-scale interfacial motion with k^{-2} scaling, while the energy of small-scale modes decays more rapidly as k^{-4} .

Our simulations reproduce the temporal characteris-

tics observed in experiments. Kymographs of equatorial fluctuations $r(\varphi,t)$ in Fig. S7a and the dynamic structure factor in Fig. 2h closely match their experimental counterparts, confirming the presence of propagating wave modes at small k. To elucidate the origin of these waves at low Reynolds number, we impose a smallamplitude deformation on the interface corresponding to a spherical harmonic mode with $(\ell, m = 0)$ (Fig. S12 and Methods). These spherical harmonic modes possess axial symmetry, and can be projected onto the meridional plane to yield a deformation wave vector $k = \ell/R$. Figure 3a shows the time evolution of interfacial deformation and fluid flow on the meridional plane following an initial perturbation at $(\ell = 5, m = 0)$. The corresponding mode amplitude is shown in Fig. 3b, indicating clear oscillation over time. The flow fields in Fig. 3a reveal the emergence of an effective inertia that underpins the selfsustained interfacial waves. Specifically, in a passive low-Reynolds-number fluid, a deformed interface generates a restoring flow that vanishes once the interface relaxes to equilibrium. By contrast, when the droplet encapsulates active bacteria, the capillary-induced flow persists even

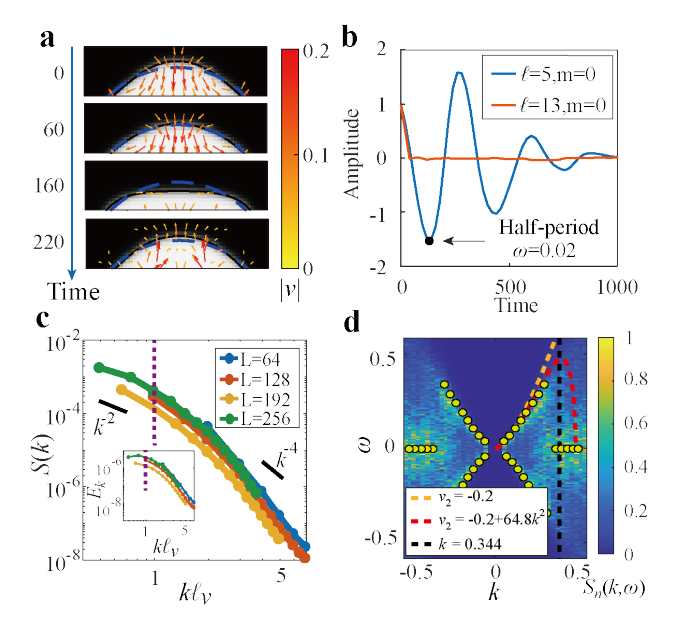


FIG. 3. Oscillatory and wave dynamics from simulations of a spherical (top) and flat (bottom) interface. (a) Interface evolution and associated flow field resulting from an initial perturbation with a spherical harmonic mode ($\ell = 5, m = 0$) on a spherical interface. The blue dashed line indicates the unperturbed shape. One-fifth of the droplet is shown for clarity. (b) Temporal evolution of the amplitudes of the $(\ell = 5, m = 0)$ and $(\ell = 13, m = 0)$ modes. The black dot denotes the corresponding frequency appearing in Fig. 2h. (c) Fluctuation spectra, S(k), obtained from 2D simulations of four flat interfaces. Inset: Mean interfacial energy E_k as a function of $k\ell_v$. The dashed lines mark $k\ell_v = 1$. The expression of E_k is procided in Sec. S3 of the SI. (d) Normalized dynamic structure factor $S_n(k,\omega)$ measured from a flat interface. The orange and red dashed lines represent the analytical results in Eq. (2) without and with the inclusion of higher-order viscosity, respectively; the black dashed line marks the threshold beyond which propagating modes disappear. The yellow dots denote characteristic frequencies extracted from simulations with specific initial conditions. All simulation parameters are given in Sec. S2 in the SI.

at the equilibrium shape, behaving as though it carried inertia. This persistent active flow then drives the interface past its equilibrium configuration and gives rise to oscillatory dynamics. Initial perturbations with large ℓ decay rapidly without oscillation (Fig. 3b), corresponding the diffusive modes peaked at zero frequency in Fig. 2h. By varying the spherical harmonic degree ℓ of the initial perturbation, we extract a characteristic oscillation frequency for each ℓ (Fig. 3b and Fig. S14c). The extracted frequencies, plotted as red dots in Fig. 2h, are consistent with $S_n(k,\omega)$ from the turbulent state, confirming that the propagating wave modes are indeed sustained by the persistent active flows. The key features of the dynamic structure factor, including wave modes at small k and the transition to diffusive modes, are robustly reproduced across a range of parameters (Fig. S18).

To verify the universality of the wave mechanism and to facilitate analytical treatment, we further use our simulations to investigate interfacial fluctuations on a flat interface separating passive and active fluids in two dimensions (Fig. S20). The fluctuation spectra of the 2D interface show a clear transition in scaling at $1/\ell_v$ (Fig. 3c), corresponding to the scale where active flows inject energy into the interface (Fig. 3c inset). The normalized dynamic structure factor $S_n(k,\omega)$ of the flat interface resembles its spherical counterpart, showing clear evidence of propagating modes at $k < k_c$ (Fig. 3d). Similarly, oscillation frequencies extracted from perturbed interfaces coincide with those from the turbulent steady state (Fig. 3d and Fig. S14d-f).

The 2D planar geometry greatly simplifies the analytical treatment [17, 59–61]. To linear order, the interface height h(x,t) is mainly driven by the normal velocity, i.e., $\partial_t h(x,t) = v_y(x,y=0,t)$. The flow fields in each phase obey the linearized TTSH equation

$$\partial_t \mathbf{v}^i = -\nabla P^i - \alpha_i \mathbf{v}^i + \nu_i \nabla^2 \mathbf{v}^i \,, \tag{1}$$

where i=1,2 denote passive and active fluids, respectively. α_i represents the effective damping coefficient, and ν_i is the effective viscosity. Here, we drop the fourth-order viscosity to further simplify analytics. Solving Eq. (1) with proper boundary conditions at the interface yields the dispersion relation of the interfacial waves, which agrees quantitatively with simulations $k < k_c$ (Fig. S21a, see Methods and Sec. S5 for details). In the limit of small α_i and $|\nu_i|k^2 \gg \omega$, both justified in Sec. S5, the dispersion relation reduces to a simple form

$$(i\tilde{\omega})^2 + \frac{1}{\tau_v}i\tilde{\omega} + \frac{1}{\tau_0^2} = 0,$$
 (2)

resembling that of damped harmonic oscillator. The interface dynamics is dominated by two characteristic time scales: the viscous damping time $\tau_v(k) = 3/[2(\nu_1 + \nu_2)]$ $\nu_2 k^2$ and the capillary-driven oscillation period $\tau_0(k) =$ $\sqrt{3/(\gamma_0 k^3)}$. Similar to the damped harmonic oscillator, oscillatory modes arise in the underdamped region, $\tau_v > \tau_0/2$. For passive droplets at low Reynolds number, viscous damping dominates so that $\tau_v \ll \tau_0$ and interfacial modes are purely diffusive. By contrast, droplets encapsulating bacteria acquire a negative effective viscosity ν_2 that can offset viscous damping, rendering the interface underdamped and reintroducing inertia effects to the interface, when the matching condition $\nu_1 + \nu_2 \sim 0$ is satisfied. Notably, oscillatory modes disappear again at high activity, where $|\nu_2|$ is sufficiently larger than ν_1 , in which case the flat interface becomes linearly unstable and fluctuations grow exponentially. The underdamped condition defines a critical wavenumber $k_c' = 3\gamma_0/(\nu_1 + \nu_2)^2$ beyond which interfacial modes become diffusive (see Sec. S4E). However, this theoretical value is larger than k_c identified from numerical simulations, reflecting the

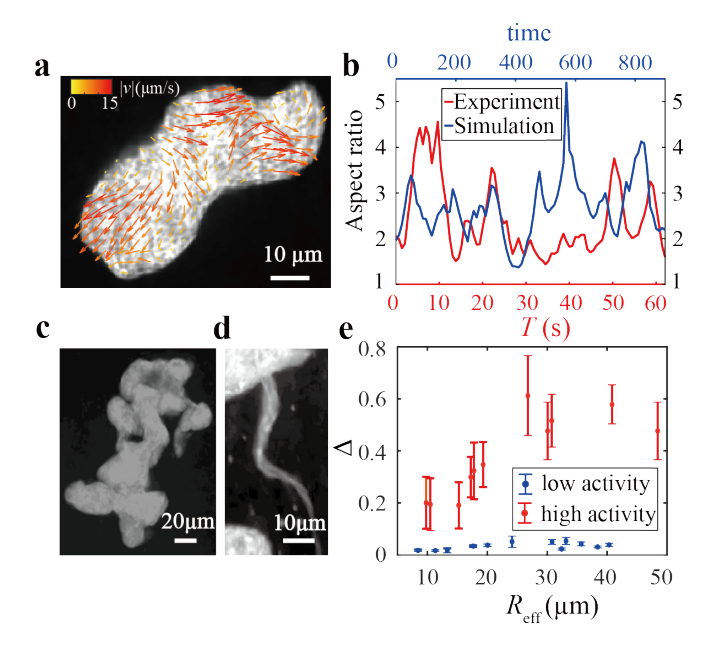


FIG. 4. Shape and dynamics of strongly deformed droplets. (a) Bacterial flow field in an elongating droplet. (b) Temporal evolution of the droplet aspect ratio in experiment (red) and simulation (blue). (c) Representative image of a droplet exhibiting a complex, highly non-spherical shape. (d) Filament-like protrusions extending from the droplet interface. (e) Normalized surface area as a function of droplet size, $R_{\rm eff}$, under low-activity (blue) and high-activity (red) conditions. $R_{\rm eff}$ is defined as $R_{\rm eff} = (3V/4\pi)^{1/3}$, where V is the droplet volume. All experimental data correspond to droplets with $\varphi_{\rm b} = 35\%$, except for the low-activity data in (e). The simulation curve in (b) corresponds to the snapshots and parameters in Fig. S23.

omission of higher-order viscosity and nonlinear dynamics in the theory. We account for these effects phenomenologically by replacing ν_2 with a k-dependent viscosity $\nu_2'(k) \equiv \nu_2(1-4\ell_v^2k^2)$, which weakens the effective active driving and suppresses propagating waves on length scales smaller than the average vortex size $2\ell_v$. With this correction, the predicted dispersion relation and cutoff wavevector k_c' both agree with the simulation results (red curve in Fig. 3d).

Large droplet deformations

When the bacterial concentration is increased to 35%, strong internal flows generate persistent protrusions that push the interface outward. The resulting deformations in turn steer the active flows, creating a positive feedback loop that amplifies droplet elongation. This coupling produces highly anisotropic droplet shapes with characteristic widths on the order of the flow correlation length, ℓ_v , as shown in Fig. 4a, Fig. S1b, Fig. S22–S25, and Movies S5–S6. The aspect ratio evolution in both experiment and simulation shows stretching beyond the Rayleigh–Plateau threshold (aspect ratio π) for sev-

eral seconds, well above the passive breakup timescale $6\eta R/\gamma_0 \sim 0.1s$ (Fig. 4b and Movie S6) [62–64]. Thus, activity suppresses capillary instabilities and dynamically stabilizes droplet shapes that would otherwise break up.

In large droplets, strong internal flows generate multiple protrusions, producing a broad spectrum of deformation modes and complex, time-evolving morphologies (Fig. 4c and Movie S7). To quantify deviations from the spherical shapes favored by surface tension, we define the normalized excess surface area, $\Delta \equiv S/S_0 - 1$, where S is the droplet surface area and S_0 is that of a volume-matched sphere. Under low-activity conditions, Δ remains near zero (Fig. 4e), consistent with nearly spherical droplets. At high activity, however, large droplets exhibit substantial excess areas, with Δ reaching ~ 0.6 , corresponding to a 60% increase in surface area relative to a sphere (Fig. S27).

At the surfaces of highly active droplets, we observe protruded filaments with widths comparable to that of single bacterium (Fig. 4d, Fig. S1d, Fig. S28–S29, and Movie S8). Within these filaments, bacteria align nematically along the filament axis (Fig. S29), indicating localized ordering that emerges from the particulate character of the suspension. These features illustrate the multiscale nature of bacterial droplets, where microscopic alignment and mesoscale flow structures coexist and jointly sculpt the interface [20, 65, 66].

Contact line, droplet motion and coarsening

When passive droplets sediment to the chamber bottom, they establish stable contact lines with the substrate, forming a contact angle of approximately 150° (Fig. S8a). Active droplets exhibit markedly different behavior. Under low-activity conditions, bacterial flows deform the contact line (Fig. 5a, Fig. 5b, Fig. S9), producing small but persistent lateral displacements on the substrate (Fig. 5c). Under high-activity conditions, droplets exhibit highly irregular contact lines, intermittent detachment, and significant lateral motion (Fig. 5d–Fig. 5f, Fig. S10). This active migration near the substrate strongly influences the coarsening dynamics (Movie S9).

To quantify this effect, we measure the spatial correlation length of fluorescence intensity fluctuations within a 40 μ m layer above the substrate. This intensity correlation length, ξ , reflects the typical droplet size near the substrate and is plotted in Fig. 5h. Consistent with the snapshots in Fig. 1b–Fig. 1d, active droplets exhibit larger ξ values than passive droplets (Fig. 5g). At late times, the mass-accumulating droplets in active samples reach significantly larger radii than in passive systems (Fig. 5h). Notably, in the high-activity regime, droplets remain highly motile and continue to coarsen (Movie S1), producing a steadily increasing ξ (Fig. 5g) and a final state dominated by a few large droplets (Fig. 1d, Fig. 5h). By contrast, in passive and low-activity systems, ξ initially grows but subsequently saturates.

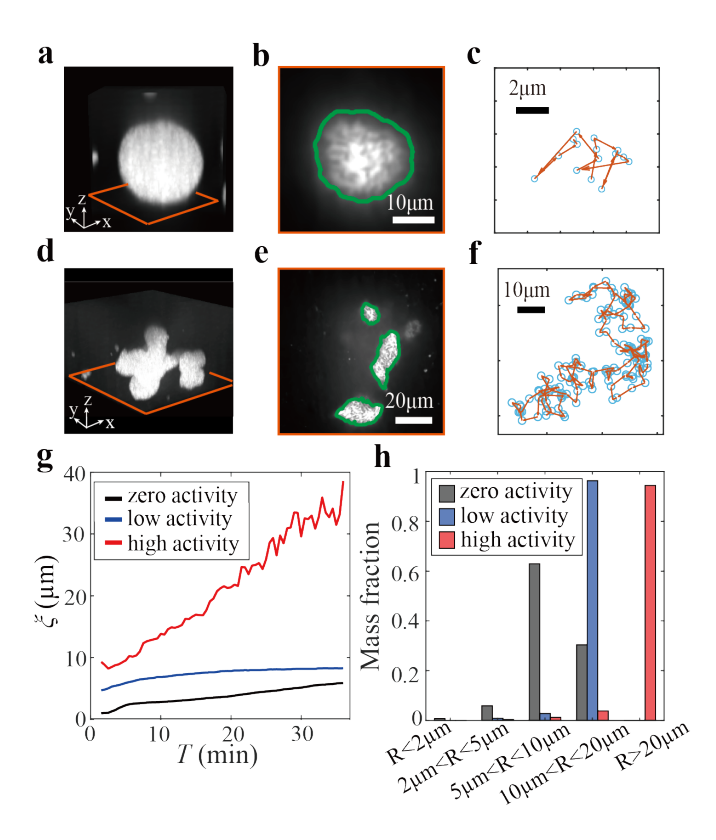


FIG. 5. Droplet motion and coarsening near the substrate. (a) Side view of a low-activity droplet with $\varphi_b=20\%$. The red contour marks the substrate position. (b) Contact line corresponding to the droplet in (a). (c) Trajectory of the droplet's center of mass in the $x\!-\!y$ plane; points are spaced by 4.7 s. (d) Side view of a high-activity droplet with $\varphi_b=35\%$, showing enhanced interfacial deformation. The red contour marks the substrate position. (e) Contact line corresponding to the droplet in (d). (f) Trajectory of the droplet's center of mass with a temporal spacing of 0.87 s. (g) Time evolution of the characteristic length of the dextran phase, $\xi(t)$, within a 40 μ m region above the substrate for the zero-, low-, and high-activity conditions. (h) Droplet size distributions at T=36 min for the zero-, low-, and high-activity groups.

Discussion and Conclusion

Activity is increasingly recognized as a powerful driver of interfacial and membrane physics, endowing soft boundaries with behaviors that have no equilibrium analogue [17–37, 66–74]. Here, we establish an experimental platform for bacteria-powered, phase-separated droplets and uncover a regime of interfacial physics in which internal activity reshapes droplet dynamics, geometry, and coarsening kinetics. In the low-activity regime, the interface develops a scale-selective fluctuation spectrum. Energy is injected at a well-defined interior length scale set by bacterial turbulence, producing a distinct spectral crossover in both experiments and simulations (Fig. 2c, Fig. 2g, Fig. S4). These scale-dependent fluctuations arise from collective bacterial flows [17], in contrast to the broadband, uncorrelated agitation generated by isolated

active units [20, 21, 23]. Beyond this spectral signature, we find that active—passive coupling restores effective inertia at vanishing Reynolds number: active stresses offset passive viscous dissipation, which dramatically reduces damping and enables underdamped, capillary-like waves on a liquid-liquid boundary (Fig. 2d, Fig. 2h, Fig. 3a, Fig. 3d). Whereas interfacial waves in active nematics are typically attributed to the nonreciprocal coupling between the nematic director and the interface [17, 67], our results reveal a hydrodynamic route based on viscosity matching between active and passive fluids. This mechanism expands the conceptual framework of active interfaces by showing that internal motility can tune the temporal character of soft boundaries from purely relaxational to oscillatory, offering design principles for wavesupporting interfaces in living and synthetic systems.

At high activity, internal stresses produce large, persistent deformations of liquid droplets (Fig. 4a, Fig. 4b). Such extreme shapes are typically unstable in liquid-liquid interfaces, where Rayleigh-Plateau instabilities promote breakup, unlike membrane-bound systems where bending rigidity prevents rupture [20, 25, 66]. Remarkably, our results show that activity not only drives giant deformations but also dynamically stabilizes highly distorted states, maintaining configurations with no passive counterpart. Turning to coarsening, activity is known to regulate domain growth and induce microphase separation in active mixtures [18, 34, 68– 70, 73]. In our gravitational geometry, activity adds an additional route to acceleration: internal flows accelerate coalescence by deforming droplets and enhancing transport while, growth to larger droplets boosts sedimentation and thus the collision rates (Fig. 5g, Fig. 5h). Together, these mechanisms establish motility as a powerful control parameter for both morphology and phaseseparation timescales in active emulsions.

Altogether, our results identify active, phase-separated droplets as a minimal system in which internal stresses dictate interfacial mechanics: they program fluctuation spectra, generate capillary-like waves at vanishing Reynolds number, stabilize strongly deformed geometries, and accelerate coarsening. These behaviors arise from generic nonequilibrium energy injection and hydrodynamic coupling, demonstrating that liquid boundaries can acquire mechanical functionality from within. In this sense, active droplets operate as self-powered mechanical compartments whose interfaces can withstand large deformation, suppress rupture, and exhibit motility, traits normally reserved for living cells. This establishes a physical pathway through which internal activity can confer shape control, transport capability, and robustness to soft matter assemblies, providing a foundation for programmable active droplets and mechanically competent artificial cells.

Conflicts of interest

There are no conflicts of interest.

Acknowledgements

We thank Shuo Guo for providing *E. coli* BW25113 strain. Discussions with Xiaqing Shi, Rui Ma, and Dahai He are highly benificial. HPZ was supported by the National Key R&D Program of China (grant no. 2021YFA0910700) and the National Natural Science Foundation of China (No. 12225410, No. 12074243). ZY was supported by the National Natural Science Foundation of China (No. 12374219), the National Key Research and Development Program of China (No. 2023YFA1407500), and the 111 project (B16029).

- * These authors contributed equally
- † Corresponding author: zhyou@xmu.edu.cn
- [‡] Corresponding author: Hepeng_zhang@sjtu.edu.cn
- [1] Needleman, D. & Dogic, Z. Active matter at the interface between materials science and cell biology. *Nature Reviews Materials* **2**, 17048 (2017).
- [2] Lv, C.-L. & Li, B. Interface morphodynamics in living tissues. Soft Matter 21, 3670–3687 (2025). Review Article.
- [3] Turlier, H. & Betz, T. Unveiling the active nature of living-membrane fluctuations and mechanics. *Annual Review of Condensed Matter Physics* **10**, 213–232 (2019).
- [4] Hyman, A. A., Weber, C. A. & Jülicher, F. Liquid-liquid phase separation in biology. *Annual Review of Cell and Developmental Biology* 30, 39–58 (2014).
- [5] Fletcher, D. A. & Mullins, R. D. Cell mechanics and the cytoskeleton. *Nature* 463, 485–492 (2010).
- [6] Pollard, T. D. & Cooper, J. A. Actin, a central player in cell shape and movement. *Science* 326, 1208–1212 (2009).
- [7] Keren, K. et al. Mechanism of shape determination in motile cells. Nature 453, 475–480 (2008).
- [8] Brochard, F. & Lennon, J. F. Frequency spectrum of the flicker phenomenon in erythrocytes. J. Phys. (France) 36, 1035–1047 (1975).
- [9] Gov, N., Zilman, A. G. & Safran, S. A. Cytoskeleton confinement and tension of red blood cell membranes. *Phys. Rev. Lett.* **90**, 228101 (2003).
- [10] Fournier, J.-B., Lacoste, D. & Raphaël, E. Fluctuation spectrum of fluid membranes coupled to an elastic meshwork: jump of the effective surface tension at the mesh size. *Phys. Rev. Lett.* 92, 018102 (2004).
- [11] Gov, N. S. & Safran, S. A. Red blood-cell membrane fluctuations and shape: controlled by atp-induced cytoskeletal defects. *Biophys. J.* 88, 1859–1874 (2005).
- [12] Gov, N. S. Active elastic network: Cytoskeleton of the red blood cell. Phys. Rev. E 75, 011921 (2007).
- [13] Turlier, H. et al. Equilibrium physics breakdown reveals the active nature of red blood cell flickering. Nat. Phys. 12, 513–519 (2016).
- [14] Schwayer, C. et al. Mechanosensation of tight junctions depends on ZO-1 phase separation and flow. Cell 179, 937–952.e18 (2019).

- [15] Kim, S., Kalappurakkal, J. M., Mayor, S. & Rosen, M. K. Phosphorylation of nephrin induces phase separated domains that move through actomyosin contraction. *Mol. Biol. Cell* 30, 2996–3012 (2019).
- [16] Wiegand, T. & Hyman, A. Drops and fibers—how biomolecular condensates and cytoskeletal filaments influence each other. *Emerging Topics in Life Sciences* 4, 247–261 (2020).
- [17] Adkins, R. et al. Dynamics of active liquid interfaces. Science 377, 768–772 (2022).
- [18] Tayar, A. M. et al. Controlling liquid-liquid phase behaviour with an active fluid. Nature Materials 22, 1401– 1408 (2023).
- [19] Zhao, L. et al. Asymmetric fluctuations and self-folding of active interfaces. Proceedings of the National Academy of Sciences 121, e2410345121 (2024).
- [20] Takatori, S. C. & Sahu, A. Active contact forces drive nonequilibrium fluctuations in membrane vesicles. *Physical Review Letters* 124, 158102 (2020).
- [21] Vutukuri, H. R. et al. Active particles induce large shape deformations in giant lipid vesicles. Nature 586, 52–56 (2020).
- [22] Keber, F. C. et al. Topology and dynamics of active nematic vesicles. Science 345, 1135–1139 (2014).
- [23] Sciortino, A. et al. Active membrane deformations of a minimal synthetic cell. Nature Physics 21, 954–962 (2025).
- [24] Park, M., Lee, K. & Granick, S. Response of vesicle shapes to dense inner active matter. Soft Matter 18, 6419–6425 (2022).
- [25] Nagard, L. L. et al. Encapsulated bacteria deform lipid vesicles into flagellated swimmers. Proceedings of the National Academy of Sciences 119, e2206096119 (2022).
- [26] Xie, K. et al. Activity induced rigidity of liquid droplets. Physical Review Letters 129, 138001 (2022).
- [27] Kokot, G., Faizi, H. A., Pradillo, G. E., Snezhko, A. & Vlahovska, P. M. Spontaneous self-propulsion and nonequilibrium shape fluctuations of a droplet enclosing active particles. *Communications Physics* 5, 91 (2022).
- [28] Zhao, Q.-H., Qi, J.-Y. & Deng, N.-N. Dna photofluids show life-like motion. *Nature Materials* 24, 935–944 (2025).
- [29] Liu, C., Cao, D., Liu, S. & Wu, Y. Nonequilibrium dynamics of membraneless active droplets. arXiv preprint arXiv:2511.04181 (2025). 2511.04181.
- [30] Ruske, L. J. & Yeomans, J. M. Morphology of active deformable 3d droplets. *Physical Review X* 11, 021001 (2021).
- [31] Tjhung, E., Marenduzzo, D. & Cates, M. E. Spontaneous symmetry breaking in active droplets provides a generic route to motility. Proceedings of the National Academy of Sciences of the United States of America 109, 12381– 12386 (2012).
- [32] Tjhung, E., Cates, M. E. & Marenduzzo, D. Contractile and chiral activities codetermine the helicity of swimming droplet trajectories. *Proceedings of the National Academy* of Sciences 114, 4631–4636 (2017).
- [33] Giomi, L. & DeSimone, A. Spontaneous division and motility in active nematic droplets. *Physical Review Let*ters 112, 147802 (2014).
- [34] Blow, M. L., Thampi, S. P. & Yeomans, J. M. Biphasic, Lyotropic, Active Nematics. *Physical Review Letters* 113, 248303 (2014).

- [35] Nejad, M. R. & Yeomans, J. M. Spontaneous rotation of active droplets in two and three dimensions. *PRX Life* 1, 023008 (2023).
- [36] Young, Y.-N., Shelley, M. J. & Stein, D. B. The many behaviors of deformable active droplets. *Mathematical Biosciences and Engineering* 18, 2849–2881 (2021).
- [37] Kawakami, S. & Vlahovska, P. M. Migration and deformation of a droplet enclosing an active particle. *Journal of Fluid Mechanics* 1007, A41 (2025).
- [38] Crowe, C. D. & Keating, C. D. Liquid-liquid phase separation in artificial cells. *Interface Focus* 8, 20180032 (2018). Publisher: The Royal Society.
- [39] Salehi-Reyhani, A., Ces, O. & Elani, Y. Artificial cell mimics as simplified models for the study of cell biology. Experimental Biology and Medicine 242, 1309–1317 (2017).
- [40] Buddingh', B. C. & van Hest, J. C. M. Artificial cells: synthetic compartments with life-like functionality and adaptivity. Accounts of Chemical Research 50, 769–777 (2017).
- [41] Spoelstra, W. K., Deshpande, S. & Dekker, C. Tailoring the appearance: what will synthetic cells look like? Current Opinion in Biotechnology 51, 47–56 (2018).
- [42] Hammer, D. A. & Kamat, N. P. Towards an artificial cell. FEBS Letters 586, 2882–2890 (2012).
- [43] Yaguchi, T. et al. Micropatterning bacterial suspensions using aqueous two phase systems. Analyst 135, 2848–2852 (2010).
- [44] Cheon, J. et al. Motility modulates the partitioning of bacteria in aqueous two-phase systems. Physical Review Letters 135, 128401 (2025).
- [45] Wei, D. et al. Scaling Transition of Active Turbulence from Two to Three Dimensions. Advanced Science 11, 2402643 (2024).
- [46] Perez-Estay, B. et al. Bacteria collective motion is scalefree. arXiv (2025). 2509.15918.
- [47] Pécréaux, J., Döbereiner, H.-G., Prost, J., Joanny, J.-F. & Bassereau, P. Refined contour analysis of giant unilamellar vesicles. The European Physical Journal E 13, 277–290 (2004).
- [48] Stottrup, B. L., Heussler, A. M. & Bibelnieks, T. A. Determination of Line Tension in Lipid Monolayers by Fourier Analysis of Capillary Waves. The Journal of Physical Chemistry B 111, 11091–11094 (2007).
- [49] Honerkamp-Smith, A. R. et al. Line tensions, correlation lengths, and critical exponents in lipid membranes near critical points. *Biophysical Journal* **95**, 236–246 (2008).
- [50] Shimobayashi, S. F., Konishi, K., Ackerman, P. J., Taniguchi, T. & Brangwynne, C. P. Critical capillary waves of biomolecular condensates. bioRxiv (2023). Preprint, not peer-reviewed.
- [51] Yue, P., Feng, J. J., Liu, C. & Shen, J. A diffuse-interface method for simulating two-phase flows of complex fluids. *Journal of Fluid Mechanics* 515, 293–317 (2004).
- [52] Dunkel, J. et al. Fluid dynamics of bacterial turbulence. Physical Review Letters 110, 228102 (2013).
- [53] Dunkel, J., Heidenreich, S., Bär, M. & Goldstein, R. E. Minimal continuum theories of structure formation in dense active fluids. New Journal of Physics 15, 045016 (2013).
- [54] Heidenreich, S., Dunkel, J., Klapp, S. H. L. & Bär, M. Hydrodynamic length-scale selection in microswimmer suspensions. *Physical Review E* 94, 020601 (2016).

- [55] Reinken, H., Klapp, S. H. L., Bär, M. & Heidenreich, S. Derivation of a hydrodynamic theory for mesoscale dynamics in microswimmer suspensions. *Physical Review* E 97, 022613 (2018).
- [56] Alert, R., Casademunt, J. & Joanny, J.-F. Active turbulence. Annual Review of Condensed Matter Physics 13, 143–170 (2022). 2104.02122.
- [57] Wensink, H. H. et al. Meso-scale turbulence in living fluids. Proceedings of the National Academy of Sciences 109, 14308–14313 (2012).
- [58] Peng, Y., Liu, Z. & Cheng, X. Imaging the emergence of bacterial turbulence: Phase diagram and transition kinetics. *Science Advances* 7, eabd1240 (2021).
- [59] Grant, M. & Desai, R. C. Fluctuating hydrodynamics and capillary waves. *Physical Review A* 27, 2577–2584 (1983).
- [60] Harden, J. L., Pleiner, H. & Pincus, P. A. Hydrodynamic surface modes on concentrated polymer solutions and gels. *Journal of Chemical Physics* 94, 5208–5221 (1991).
- [61] Flekkøy, E. G. & Rothman, D. H. Fluctuating hydrodynamic interfaces: Theory and simulation. *Physical Re*view E 53, 1622–1643 (1996).
- [62] Rayleigh, L. Xvi. on the instability of a cylinder of viscous liquid under capillary force. The London, Edinburgh, and Dublin Philosophical Magazine and Journal of Science 34, 145–154 (1892).
- [63] Plateau, J. Statique expérimentale et théorique des liquides soumis aux seules forces moléculaires, vol. 2 (Gauthier-Villars, 1873).
- [64] Pekker, L. On Plateau–Rayleigh Instability of a Cylinder of Viscous Liquid. *Journal of Imaging Science* and Technology 62, 040405-1-040405-8 (2018).
- [65] Hickl, V. & Juarez, G. Tubulation and dispersion of oil by bacterial growth on droplets. Soft Matter 18, 7217– 7228 (2022).
- [66] Prasad, M. et al. Alcanivorax borkumensis biofilms enhance oil degradation by interfacial tubulation. Science 381, 748–753 (2023).
- [67] Gulati, P., Caballero, F., Kolvin, I., You, Z. & Marchetti, M. C. Traveling waves at the surface of active liquid crystals. Soft Matter 20, 7703-7714 (2024).
- [68] Cates, M. E. & Nardini, C. Active phase separation: new phenomenology from non-equilibrium physics. Reports on Progress in Physics 88, 056601 (2025).
- [69] Caballero, F. & Marchetti, M. C. Activity-Suppressed Phase Separation. *Physical Review Letters* 129, 268002 (2022).
- [70] Bhattacharyya, S. & Yeomans, J. M. Phase separation driven by active flows. *Physical Review Letters* 130, 238201 (2023).
- [71] Li, Y. & ten Wolde, P. R. Shape transformations of vesicles induced by swim pressure. *Physical Review Letters* 123, 148003 (2019).
- [72] Carenza, L. N., Hoffmann, L. A., Eckert, J. & Giomi, L. Topological defect-mediated morphodynamics of active-active interfaces. Proceedings of the National Academy of Sciences of the United States of America 119, e2122494119 (2022).
- [73] Fausti, G., Tjhung, E., Cates, M. E. & Nardini, C. Capillary interfacial tension in active phase separation. *Physical Review Letters* 127, 068001 (2021).
- [74] Dignon, G. L. et al. Polymer physics of intracellular phase transitions. Nature Physics 14, 117–126 (2018).

- [75] Gurtin, M. E., Polignone, D. & Vinals, J. Two-phase binary fluids and immiscible fluids described by an order parameter. *Mathematical Models and Methods in Applied* Sciences 6, 815–831 (1996).
- [76] Yue, P., Zhou, C., Feng, J. J., Ollivier-Gooch, C. F. & Hu, H. H. Phase-field simulations of interfacial dynamics in viscoelastic fluids using finite elements with adaptive meshing. *Journal of Computational Physics* 219, 47–67 (2006).
- [77] Kim, J. Phase-field models for multi-component fluid flows. Communications in Computational Physics 12, 613–661 (2012).

Methods Bacterial cultivation

We use *E. coli* BW25113 as the active component. Cells are cultured overnight at 37.0 °C in Terrific Broth (TB), diluted 1:100 in fresh TB medium, and grown at 30.0 °C for 5 hours. After centrifugation and washing with motility buffer, the cells are resuspended and prepared for further experiments.

Phase-separating solution

The phase-separating mixture is prepared by dissolving dextran (DEX) and polyethylene glycol (PEG) at equal initial mass concentrations in motility buffer. Fluorescein-labeled dextran (D1844, 40,000 MW) is added at a final concentration below 0.1% (w/w) to enable fluorescent visualization of the dextran-rich phase. The interfacial tension of the resulting liquid–liquid interface is measured to be 7 μ N/m.

Sample preparation

To set the desired bacterial volume fraction, we mix 200 μ L of PEG-rich phase, 10 μ L of DEX-rich phase, and either 5 μ L (low activity, $\varphi_b = 20\%$) or 8 μ L (high activity, $\varphi_b = 35\%$) of dense bacterial suspension. The bacterial volume fraction is estimated by scanning the droplets under a 240× SORA mode on a confocal microscope and manually counting bacteria. Samples are sealed in circular chambers (radius: 2.5 mm) assembled from double-sided adhesive tape sandwiched between two glass slides. The chamber height is set to 200 μ m for small droplets and coarsening measurements, and to 600 μ m for samples containing droplets larger than 100 μ m in radius, preventing contact with the upper slide.

Imaging

Imaging is performed using a Nikon spinning disk confocal microscope (CSU-W1). Flow-field measurements

and contour extraction for droplets with radii below 100 μm use a 60× water-immersion objective. Droplets larger than 100 μm are imaged using a 20× objective.

Data analysis

The acquired images are preprocessed using the 'denoise.ai' module in NIS-Element Viewer. Droplet contours are identified in MATLAB via binarization. Morphological properties of 3D droplets—including surface area, volume, and aspect ratio—are extracted using MATLAB's regionprops3.

The 2D deformation field $r(\varphi,t)$ is defined as the radial distance from each contour pixel to the center of mass of the 2D cross-section. Fluctuation spectra are computed using discrete Fourier transforms. The dynamic structure factor (DSF) is calculated by performing a spatial-temporal Fourier transform after interpolating the boundary points (r_i, φ_i) at each time t onto a uniform grid. Because the fluctuation spectrum decays with increasing k, the DSF is dominated by the largest spatial scales (Fig. S5–S6). To consistently compare modes with different amplitudes, we normalize each DSF curve at fixed k by its maximum value. Specifically, at $k = k_i$, the normalized DSF $S_n(k_i, \omega)$ is defined as

$$S_n(k_i, \omega) = \frac{S(k_i, \omega)}{\max_{\omega} S(k_i, \omega)}.$$
 (3)

Numerical simulation

The model comprises a phase field $\phi(\mathbf{x},t)$ and an incompressible flow field \mathbf{v} with $\nabla \cdot \mathbf{v} = 0$. The phase field $\phi(\mathbf{x},t)$ evolves according to an advective Cahn–Hilliard equation:

$$(\partial_t + \mathbf{v} \cdot \nabla) \phi = \Gamma_\phi \nabla^2 \mu, \tag{4}$$

where Γ_{ϕ} sets the relaxation rate. The chemical potential $\mu \equiv \delta F_{\phi}/\delta \phi$ is derived from a standard Ginzburg–Landau free energy:

$$F^{\phi} = \int_{\mathbf{r}} \left[\frac{a_{\phi}}{4} \phi^2 (1 - \phi)^2 + \frac{k_{\phi}}{2} |\nabla \phi|^2 \right] d\mathbf{r}. \tag{5}$$

The free energy drives spontaneous phase separation into $\phi = 1$ (active) and $\phi = 0$ (passive) domains, separated by an interface across which ϕ varies smoothly.

The flow field \mathbf{v} is governed by the Toner-Tu-Swift-Hohenberg (TTSH) equation [52–55]:

$$\partial_t \mathbf{v} + \lambda_0 \mathbf{v} \cdot \nabla \mathbf{v} = -\nabla p^* - \alpha \left(\phi - \frac{\mathbf{v}^2}{v_0^2} \right) \mathbf{v}$$

$$+ \nu \nabla^2 \mathbf{v} - \zeta \nabla^4 \mathbf{v} + \mu \nabla \phi.$$
(6)

The coefficients in Eq. (6) are set to depend on ϕ to disable activity in the passive phase $\phi = 0$. Specifically, we choose the advection coefficient as $\lambda_0 = 1 - S_v \phi$, so that it equals 1 in the passive phase and $1 - S_v$ in the active phase, reflecting active self-advection. The parameter S_v is positive for pusher-type swimmers such as the bacteria in our experiment. The modified pressure $p^* = (p - \phi S_v \mathbf{v}^2/d)$ includes an active contribution in d-dimensional space. α and v_0 set the characteristic flow speed, enforcing $v \approx 0$ in the passive phase and $v \approx v_0$ in the active phase. Bacterial activity also enters through an activity-dependent viscosity,

$$\nu = [\nu_1(1-\phi) + \nu_2\phi],$$

where ν_1 and ν_2 are the passive and active viscosity, respectively. A negative ν_2 can destabilize the flow and, together with the stabilizing fourth-order viscosity, it sets a characteristic velocity correlation length $\sqrt{\zeta/|\nu_2|}$ and velocity scale $v_{\zeta} = \sqrt{-\nu_2^3/\zeta}$. Interfacial tension enters via the term $\mu\nabla\phi$ [75–77]. The parameter values and the specific simulation setting are provided in the SI.

Theory for a flat interface

In the analytical model, we treat the horizontal interface as a sharp boundary rather than a diffuse phase field. The interface deformation is described by a height field h(x,t), separating a passive fluid (fluid 1, above) from an active fluid (fluid 2, below). Activity is incorporated as a negative effective viscosity in the active layer, consistent with the TTSH framework. The linearized hydrodynamic equations in each fluid are given by

$$\partial_t \mathbf{v}^i = -\nabla P^i + \alpha_i \mathbf{v}^i + \nu_i \nabla^2 \mathbf{v}^i, \quad \nabla \cdot \mathbf{v}^i = 0, \quad (7)$$

for i = 1, 2. Considering small deformations, the kinematic boundary condition relates the interface deformation to the vertical velocity:

$$\partial_t h = v_u, \tag{8}$$

evaluated at the interface. Continuity of velocity and stresses balance at the interface impose the boundary conditions

$$[\mathbf{v}]_0 = 0,$$

$$[T_{xy}]_0 = 0,$$

$$[T_{yy}]_0 = -\gamma_0 \partial_x^2 h(x, t),$$
(9)

where $[s(x)]_0 \equiv s(x,0^-) - s(x,0^+)$ denotes the variation of quantity s across the interface, $\mathbf{T}^i = \nu_i \left(\nabla \mathbf{v}^i + \nabla \mathbf{v}^{iT} \right) - P^i \mathbf{I}$ are the stress tensor for each flow, \mathbf{I} is the unit tensor. Solving Eqs.(7)-(9) yields the dispersion relation for the interface:

$$i\tilde{\omega} = -\frac{[\nu_1(1+\beta_1) + \nu_2(1+\beta_2)]\gamma_0 k}{f_1\nu_1^2 + f_2\nu_1\nu_2 + f_3\nu_2^2}.$$
 (10)

where

$$f_1 = -1 + 3\beta_1 + \beta_1^2 + \beta_1^3,$$

$$f_2 = 2 - (\beta_1 + \beta_2) + \beta_1^2 + \beta_2^2 + 4\beta_1\beta_2 + \beta_1\beta_2(\beta_1 + \beta_2),$$

$$f_3 = -1 + 3\beta_2 + \beta_2^2 + \beta_2^3,$$

and $\beta_i = \sqrt{1 + \frac{i\tilde{\omega} - \alpha_i}{\nu_i k^2}}$. This resulting dispersion relation agrees quantitatively with that from numerical simulations at small wavenumber (Fig. 3d, Fig. S21).